MNRAS 000, 1–12 (2019) Preprint 18th February 2020 Compiled using MNRAS LATEX style file v3.0

# New constraints on the magnetization of the cosmic web using LOFAR Faraday rotation observations

S. P. O'Sullivan[1,2⋆], M. Brüggen[1], F. Vazza[3,1,4], E. Carretti[4], N. Locatelli[3,4], C. Stuardi[3,4], V. Vacca[5], T. Vernstrom[6], G. Heald[6], C. Horellou[7], T. W. Shimwell[8,9], M. J. Hardcastle[10], C. Tasse[11], H. Röttgering[9]

[1] *Hamburger Sternwarte, Universität Hamburg, Gojenbergsweg 112, Hamburg 21029, Germany.*
[2] *School of Physical Sciences and Centre for Astrophysics & Relativity, Dublin City University, Glasnevin, D09 W6Y4, Ireland.*
[3] *Dipartimento di Fisica e Astronomia, Universitá di Bologna, Via Gobetti 92/3, 40121, Bologna, Italy.*
[4] *Istituto di Radio Astronomia, INAF, Via Gobetti 101, 40121 Bologna, Italy.*
[5] *INAF - Osservatorio Astronomico di Cagliari, Via della Scienza 5, I-09047 Selargius (CA), Italy.*
[6] *CSIRO Astronomy and Space Science, PO Box 1130, Bentley WA 6102, Australia.*
[7] *Dept. of Space, Earth and Environment, Chalmers University of Technology, Onsala Space Observatory, SE-43992 Onsala, Sweden.*
[8] *ASTRON, the Netherlands Institute for Radio Astronomy, Postbus 2, 7990 AA, Dwingeloo, The Netherlands.*
[9] *Leiden Observatory, Leiden University, PO Box 9513, NL-2300 RA Leiden, The Netherlands.*
[10] *Centre for Astrophysics Research, School of Physics, Astronomy and Mathematics, University of Hertfordshire, College Lane, Hatfield AL10 9AB, UK.*
[11] *GEPI & USN, Observatoire de Paris, Université PSL, CNRS, 5 Place Jules Janssen, 92190 Meudon, France.*



Accepted –. Received –; in original form –.

**ABSTRACT**

Measuring the properties of extragalactic magnetic fields through the effect of Faraday rotation provides a means to understand the origin and evolution of cosmic magnetism. Here we use data from the LOFAR Two-Metre Sky Survey (LoTSS) to calculate the Faraday rotation measure (RM) of close pairs of extragalactic radio sources. By considering the RM difference ($\Delta$RM) between physical pairs (e.g. double-lobed radio galaxies) and non-physical pairs (i.e. close projected sources on the sky), we statistically isolate the contribution of extragalactic magnetic fields to the total RM variance along the line of sight. We find a difference in the rms of $\Delta$RM between non-physical and physical pairs of $0.4 \pm 0.3$ rad m$^{-2}$, and a difference in the corresponding median $|\Delta\mathrm{RM}|$ values of $0.3 \pm 0.4$ rad m$^{-2}$. This enables us to place an upper limit on the co-moving cosmological magnetic field strength of $B < 2.5$ nG on Mpc scales. This limit is obtained by exploring a wide range of input magnetic field strengths in a model of cosmic over-densities that realistically reflects the observed matter inhomogeneities on large scales. We also compare the LOFAR RM data with a suite of cosmological MHD simulations, that explore different magnetogenesis scenarios. Both magnetization of the large scale structure by astrophysical processes such as galactic and AGN outflows, and simple primordial scenarios with seed field strengths of $B \lesssim 0.5$ nG cannot be rejected by the current data, while stronger primordial fields or models with dynamo amplification in filaments are disfavoured. In general, LOFAR polarized sources are typically located in regions of the Universe with low RM variance, making them excellent probes of the weak magnetization of cosmic filaments and voids far from galaxy cluster environments.

**Key words:** techniques: polarimetric – galaxies:active

## 1 INTRODUCTION

Uncovering the origin and understanding the evolution of cosmic magnetic fields is one of the key science goals for present and future radio telescopes (e.g. Gaensler et al. 2004; Akahori et al. 2018). In addition to understanding the influence of magnetic fields on a range of different astrophysical scales, these studies can provide important information on the physics of the early Universe (Widrow et al. 2012). In particular, detecting the presence of magnetic fields in cosmic filaments and voids can provide important constraints on magnetogenesis scenarios (Durrer & Neronov 2013; Subramanian 2016), mainly because they are not as strongly mod-

⋆ E-mail: shane.osullivan@dcu.ie

ified as the magnetic fields in galaxies and galaxy cluster environments. Direct detection of the non-thermal synchrotron emission associated with fields in cosmic filaments may be possible (Vacca et al. 2018; Vazza et al. 2019), while an alternative approach is to use the Faraday rotation of linearly polarized radio sources to measure the field strength in thermal magnetized plasma along the line of sight (Kronberg & Perry 1982; Oren & Wolfe 1995; Kolatt 1998; Stasyszyn et al. 2010; Akahori et al. 2014). This approach should also be possible in future large surveys of Fast Radio Bursts (FRB), provided that thousands of FRB rotation measures will be available (e.g. Hackstein et al. 2019).

The magnetic field properties of galaxies and the intergalactic medium in groups and clusters of galaxies are well studied (e.g. Carilli & Taylor 2002; Laing et al. 2008; Beck 2015; van Weeren et al. 2019). However, the magnetic field properties of the pristine gas far outside galaxy clusters in filaments and voids are poorly constrained, with upper limits ranging from tens of nano-gauss (Ravi et al. 2016; Vernstrom et al. 2019) and less (Blasi et al. 1999; Planck Collaboration et al. 2016a; Pshirkov et al. 2016; Hackstein et al. 2016; Bray & Scaife 2018) to lower limits of $\sim 10^{-17}$ G (Neronov & Vovk 2010; Tavecchio et al. 2011; Dermer et al. 2011; Dolag et al. 2011; Taylor et al. 2011). Improving our understanding of the strength and morphology of these fields will help to discriminate between competing models for the origin of cosmic magnetism, such as a primordial origin (Grasso & Rubinstein 2001; Widrow 2002; Kulsrud & Zweibel 2008) or at later times through AGN and/or galactic outflows (Zweibel & Heiles 1997; Furlanetto & Loeb 2001; Widrow 2002; Beck et al. 2013). Most notably, the fall off in field strength with distance from dense regions of the Universe is less steep in the case of a primordial origin compared to a later 'magnetic pollution' through outflows (Donnert et al. 2009; Vazza et al. 2017).

Assessing the magnetisation of the Universe at large scales is also crucial for the testing of models of dark matter. The presence of significant large-scale magnetic fields has been suggested as a possible explanation for the puzzling lack of infrared absorption in the observed spectra of distant blazars (e.g. Tavecchio et al. 2012; Horns et al. 2012). Axion-like particles (ALPs) are a promising candidate for dark matter (Raffelt & Stodolsky 1988; Csáki et al. 2003) and they are predicted to oscillate into high-energy photons (and back) in the presence of background magnetic fields, reducing the effective opacity of emitted $\gamma$-ray photons (Horns et al. 2012). Photon-ALP oscillations are possible for lines of sight crossing structures with $\sim 1-10$ nG on scales of a few $\sim$ Mpc (Montanino et al. 2017).

The focus of this paper is on using the Faraday rotation measure (RM) of a sample of extragalactic radio sources to constrain the properties of the intergalactic magnetic field (IGMF) on large scales. This approach probes the thermal gas density-weighted field strength along the line of sight, where

$$\mathrm{RM}_{[\mathrm{rad\ m^{-2}}]} = 0.812 \int_{\mathrm{source}}^{\mathrm{telescope}} n_{e\ [\mathrm{cm^{-3}}]}\ B_{\parallel\ [\mu\mathrm{G}]}\ dl_{\ [\mathrm{pc}]} \qquad (1)$$

with $B_\parallel$ representing the line-of-sight magnetic field strength, $n_e$ the free electron number density, and $l$ the path length through the magnetoionic medium. This is complementary to other radio studies which attempt to detect the faint synchrotron emission from relativistic electrons in the cosmic web between clusters of galaxies (e.g. Brown et al. 2017; Vernstrom et al. 2017; Vacca et al. 2018; Botteon et al. 2018; Govoni et al. 2019).

In order to assess the contribution of the IGMF to the RM, we need to study the contributions to the RM along the entire line of sight. For a statistical sample of background polarized radio sources, we are primarily concerned with the RM variance generated from extragalactic Faraday rotating material ($\sigma^2_{\mathrm{RM,ex}}$) that can be local or internal to the radio source itself or from the intergalactic medium on large scales. Furthermore, there is a large contribution from the interstellar medium (ISM) of the Milky Way ($\sigma^2_{\mathrm{RM,MW}}$), and a small contribution from the time-variable RM of the Earth's ionosphere ($\sigma^2_{\mathrm{RM,ion}}$), in addition to measurement errors ($\sigma^2_{\mathrm{RM,err}}$). The total RM variance is then

$$\sigma^2_{\mathrm{RM}} = \sigma^2_{\mathrm{RM,ex}} + \sigma^2_{\mathrm{RM,MW}} + \sigma^2_{\mathrm{RM,ion}} + \sigma^2_{\mathrm{RM,err}}\,. \qquad (2)$$

The majority of recent investigations of RM variance have been conducted at 1.4 GHz, mainly due to the catalog of 37,543 RMs produced from the NRAO VLA Sky Survey data (NVSS; Condon et al. 1998; Taylor et al. 2009). Most investigations have used this catalog to study the properties of the Milky Way (e.g. Harvey-Smith et al. 2011; Stil et al. 2011; Oppermann et al. 2012; Purcell et al. 2015; Hutschenreuter & Enßlin 2019). However, Schnitzeler (2010) and Oppermann et al. (2015) modelled both the Galactic and extragalactic RM variance and found a best-fitting extragalactic RM variance of $\sim 7$ rad m$^{-2}$. Recently, Vernstrom et al. (2019) conducted an innovative study of close pairs of extragalactic RMs to isolate an extragalactic RM variance of $\sim 5$ to 10 rad m$^{-2}$. The RM variance local to radio sources has been well studied for individual objects, typically in groups or clusters of galaxies where the hot, magnetized intracluster gas can dominate the RM variance (e.g. Laing et al. 2008). However, the contribution of Faraday rotating material directly related to the radio sources themselves can be significant in some cases (e.g. Rudnick & Blundell 2004; O'Sullivan et al. 2013; Anderson et al. 2018; Banfield et al. 2019; Knuettel et al. 2019). Importantly, since the RM variance local to radio sources can vary from 10's to 1000's of rad m$^{-2}$, isolating a population of low RM variance sources is a key objective for experiments that aim to probe foreground RM screens with high precision (Rudnick 2019). The ionospheric RM must also be considered (Sotomayor-Beltran et al. 2013) since the typical contribution is of $O(1$ rad m$^{-2})$, which is similar to or larger than the signal from the IGMF that we want to probe.

In this paper, we present an RM study in quite a different regime for Faraday rotation, using the Low Frequency Array (LOFAR; van Haarlem et al. 2013) at 150 MHz. In particular, we use data from the ongoing LOFAR Two-Metre Sky Survey (LoTSS; Shimwell et al. 2019) from 120 to 168 MHz. This provides a wavelength-squared coverage more than 600 times that of the NVSS. Since the accuracy with which one can measure Faraday rotation depends on the wavelength-squared coverage, the advantage of RM studies at m-wavelengths is a dramatically higher precision on individual RM measurements (O'Sullivan et al. 2018b; Van Eck et al. 2018; Neld et al. 2018). However, the effect of Faraday depolarization increases substantially at long wavelengths, and while this provides important information on the properties of the magnetic field, it also means that a smaller fraction of radio sources are polarized at a level which can be detected (e.g. Farnsworth et al. 2011). This means that to reach a comparable polarized source density on the sky, observations at metre wavelengths need to be much deeper than cm-wavelengths (O'Sullivan et al. 2018a). To date, the majority of polarized sources at m-wavelengths have been large FRII radio galaxies (e.g. Van Eck et al. 2018), whose polarized hotspots and/or outer lobe regions extend well beyond the host galaxy environment, making them excellent probes of the IGMF and ideal for this project.

In studying the extragalactic RM with these data, we follow

the strategy of Vernstrom et al. (2019), hereafter V19, of taking the RM difference between close pairs (< 20 arcmin) and then separating the samples into physical and non-physical (or random) pairs. The physical pairs are typically double-lobed radio galaxies, while the non-physical pairs are sources that are close in projection on the sky but physically located at different redshifts. The key insight upon which this experiment is based is that the RM variance due to the Milky Way should vary with pair angular separation in a similar manner for the physical and non-physical pairs, while the extragalactic RM variance due to the IGMF is expected to be larger for the non-physical pairs because of the much larger cosmic separation along the line of sight.

In Section 2, we describe the observational data and our classification scheme. The observational results are presented in Section 3. Two approaches to placing model limits on intergalactic magnetic fields are described in Section 4, while a discussion of the implications are given Section 5, followed by the conclusions in Section 6. Throughout this paper, we assume a ΛCDM cosmology with $H_0 = 67.8$ km s$^{-1}$ Mpc$^{-1}$, $\Omega_M = 0.308$ and $\Omega_\Lambda = 0.692$ (Planck Collaboration et al. 2016b).

## 2 DATA

The LoTSS is an ongoing survey of the northern sky with the LOFAR High Band Antennas, producing total intensity images and catalogs with an angular resolution of ∼6 arcsecond at 150 MHz (Shimwell et al. 2019). From the second data release (DR2) survey pipeline (Tasse et al. 2020, in prep), polarization data products (Stokes $Q$, $U$ and $V$) are also being produced at an angular resolution of 20 arcseconds. In this work we make use of the Stokes $Q$ and $U$ data to find linearly polarized radio sources and derive their Faraday rotation measure (RM) values.

The polarization data used here has a frequency range of 120 to 168 MHz with a channel bandwidth of 97.6 kHz. In order to efficiently find linearly polarized radio sources, we employ the technique of RM synthesis (Burn 1966; Brentjens & de Bruyn 2005) where one takes a Fourier transform of the complex linear polarization vector, $\boldsymbol{P}(\lambda^2)$, defined as

$$\boldsymbol{P}(\lambda^2) = \int_{-\infty}^{\infty} \boldsymbol{F}(\phi)\, e^{2i\phi\lambda^2}\, d\phi, \tag{3}$$

to obtain the Faraday dispersion function, $\boldsymbol{F}(\phi)$, which provides the distribution of polarized emission as a function of Faraday depth ($\phi$) along the line of sight. In our case, the Faraday depth of the peak of $|\boldsymbol{F}(\phi)|$ is taken as the RM of the source. The LoTSS data provides an RM resolution of ∼1.15 rad m$^{-2}$ with a maximum scale of ∼1.0 rad m$^{-2}$ (i.e. no sensitivity to resolved Faraday depth structures), and a maximum |RM| of ∼170 rad m$^{-2}$ (up to ∼450 rad m$^{-2}$ with half the sensitivity). The time-variable absolute ionospheric RM correction was applied using RMEXTRACT[1] as part of the standard PREFACTOR pipeline (e.g. de Gasperin et al. 2019). Residual ionospheric RM correction errors of ∼0.1 to 0.3 rad m$^{-2}$ are expected across a single 8 hr observation (Sotomayor-Beltran et al. 2013).

The polarization catalog is produced by running RM synthesis[2] on the Stokes $Q$ and $U$ images for each survey pointing out to a radius of 2 degrees from the pointing centre. The catalog used here is produced from 268 survey pointings which, considering the large overlap between adjacent pointings, covers a sky area of ∼2000 square degrees. The pointings used were not from a single contiguous sky area but were chosen from DR2 pointings that had been processed up to 2019 May 1. The pointings come from two (partially covered) areas of the sky, from RA of 7 to 19 hrs with Dec from 25 to 70°, and RA of 23 to 3 hrs with Dec from 10 to 40°. The large overlap between pointings means that the same polarized sources are often found in multiple pointings. These duplicate sources were identified and only the source closest to a pointing centre was retained. The Faraday depth range was limited to ±120 rad m$^{-2}$ with a sampling of 0.3 rad m$^{-2}$, mainly due to computer processing and storage limitations. Searching over a larger Faraday depth range (with a finer frequency channelisation) will be required to find sources in regions of the sky with high mean RM values, such as at low Galactic latitudes. A polarized source was cataloged if the peak in the Faraday dispersion function (FDF) was greater than 8 times the average noise in $Q$ and $U$ (i.e. $\sigma_{QU}$, calculated from the rms of the wings of the real and imaginary parts of the FDF at >100 rad m$^{-2}$). For an $8\sigma_{QU}$ limit we expect a false detection rate of ∼$10^{-4}$, compared to $5\sigma_{QU}$ where it may be as high as ∼4% (George et al. 2012). The $Q$ and $U$ frequency spectra were extracted at the source location and RM synthesis[3] was applied with a finer sampling of 0.1 rad m$^{-2}$. The catalogued RM value was obtained from fitting a parabola to the amplitude of the complex FDF. The error in each RM value was calculated in the standard way (e.g. Brentjens & de Bruyn 2005) as the RM resolution divided by twice the signal to noise (i.e. in our case this is ∼ $0.58\sigma_{QU}/P$), where $P$ is the peak polarized intensity in the FDF after correction for the polarization bias following George et al. (2012). polarized sources in the Faraday depth range of −3 to +1 rad m$^{-2}$ were mainly discarded due to the presence of substantial contamination from instrumental polarization, which is shifted from 0 rad m$^{-2}$ by the ionospheric RM correction. The focus on this work is to obtain an initial catalog of close RM pairs. A more complete LOFAR RM catalog is under construction with more uniform sky coverage, in addition to the inclusion of sources without a close RM pair (O'Sullivan et al. 2020, in preparation).

### 2.1 Classification of RM pairs

To obtain an initial sample of LOFAR RM pairs, we cross-matched the preliminary LOFAR RM catalog (∼1000 candidate polarized sources over ∼2000 sq. deg.) with itself, including only pairs with separations ≤ 20 arcminutes. After removing self-matches, and limiting the minimum separation to 0.33 arcmin (i.e. the angular resolution of the data of 20 arcsec), in addition to further quality assurance checks, we were left with 349 pairs. This matches the approach of V19, except for the minimum separation, which was limited to 1.5 arcmin in their study. All LOFAR pairs were restricted to come from the same pointing to avoid the systematic RM errors introduced by the different ionosphere corrections for different pointings. In fact, taking the RM difference between sources within the same pointing (as we describe later) removes the majority of the residual RM variance from the ionospheric RM correction, modulo direction-dependent variations on scales < 20 arcmin (de Gasperin et al. 2018), leaving mainly the measurement errors from the observational noise remaining. This means there is a more

[1] https://github.com/lofar-astron/RMextract
[2] https://github.com/mrbell/pyrmsynth
[3] https://github.com/CIRADA-Tools/RM

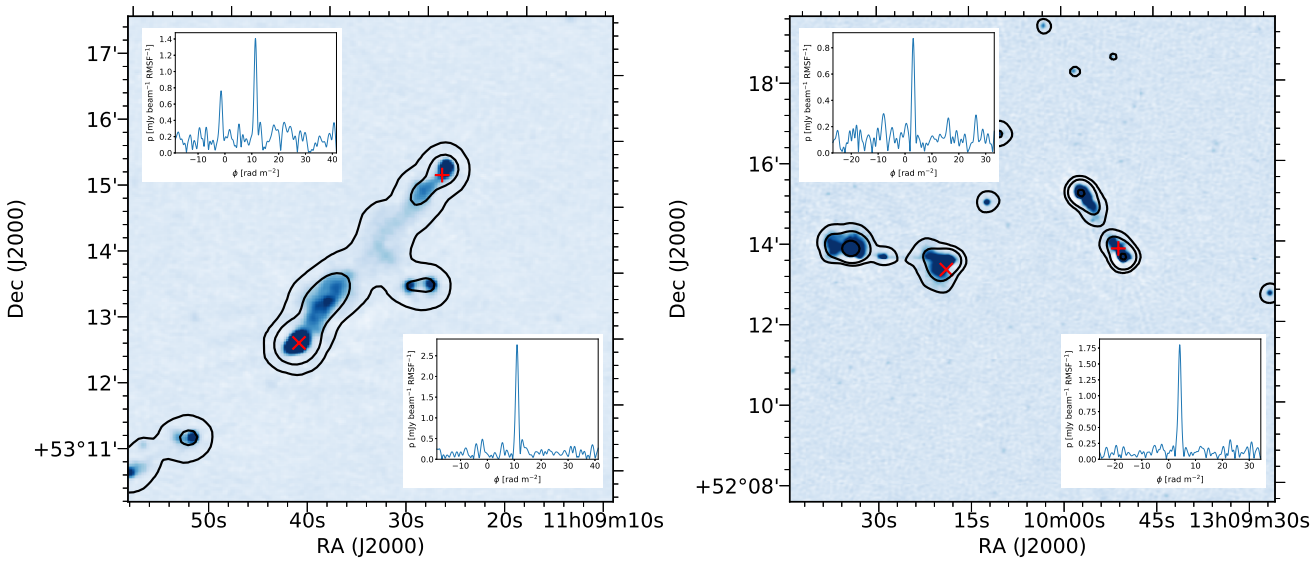


**Figure 1.** Example of a physical RM pair (left) and a non-physical, random RM pair (right). The cross and plus symbols represent the location of the peak polarized intensity from which the RM value is taken. The contours outline the total intensity emission at an angular resolution of 20 arcsec, which is the same resolution as the corresponding polarization data. The colorscale shows the 6 arcsec total intensity emission, used for the classification into physical and random pairs. The insets show the Faraday spectra from the location of the cross and plus symbols in the top left and bottom right, respectively.

precise measurement of the RM difference between pairs compared to the individual uncertainty on any one RM measurement.

Visual inspection was used to separate sources into physical pairs (part of the same extragalactic radio source, e.g. two lobes) and non-physical, random pairs (i.e. physically unrelated sources projected close to each other on the sky). Classification of sources into physical and random pairs was done by S. P. O'Sullivan. This classification task was straightforward due to the high fidelity LoTSS Stokes $I$ images available at both 20 and 6 arcsecond resolution. All pairs are at Galactic latitude $|b| > 20$ degrees, with no obvious clustering of physical or random pairs in particular parts of the sky. A Kolmogorov-Smirnov (KS) test provides no evidence for the two samples having a different underlying distribution in Galactic latitude ($p = 0.2$). The highest number of pairs for a single catalog source is 4, with a median of 1. Examples of physical and random pairs are shown in Fig. 1. Approximately 40% of the random pairs have a compact source in the pair, while the resolved physical pairs are exclusively double-lobed radio galaxies.

### 2.2 The RM difference in pairs

We are interested in investigating the difference in RM ($\Delta\mathrm{RM} = \mathrm{RM}_1 - \mathrm{RM}_2$) between pairs of sources (i.e. physical or random), in addition to the behaviour as a function of the angular separation ($\Delta\theta$). Since the RM difference can be positive or negative, we expect a mean $\Delta$RM of zero for large samples. Therefore, we calculate the root-mean-squared (rms) in $\Delta$RM as

$$\Delta\mathrm{RM}_{\mathrm{rms}} \equiv \sqrt{\langle(\Delta\mathrm{RM})^2\rangle} = \sqrt{\frac{1}{N}\sum_i (\mathrm{RM}_1 - \mathrm{RM}_2)_i^2}\,. \quad (4)$$

This is equivalent to $\sigma_{\mathrm{RM}}$ in Eqn. 2 in the case that the mean RM tends to zero for large samples. The RM variance contributed by the measurement errors can be subtracted from the total variance to analyse the astrophysical signal. We calculate this term from the quadrature sum of the errors on the individual RM measurements. Unless otherwise stated, the variance from measurement errors have been subtracted from the quoted $\Delta\mathrm{RM}_{\mathrm{rms}}$ values. The residual RM error from the ionosphere, which is typically larger than the measurement error based solely on the signal to noise, is accounted for by taking the RM difference between pairs in addition to restricting the pairs to the same observational pointing. For small samples or in the presence of outliers, the median can be a more robust statistic. Therefore, in our analysis we also consider the median of the absolute values of the RM difference (i.e. $|\Delta\mathrm{RM}|_{\mathrm{median}}$).

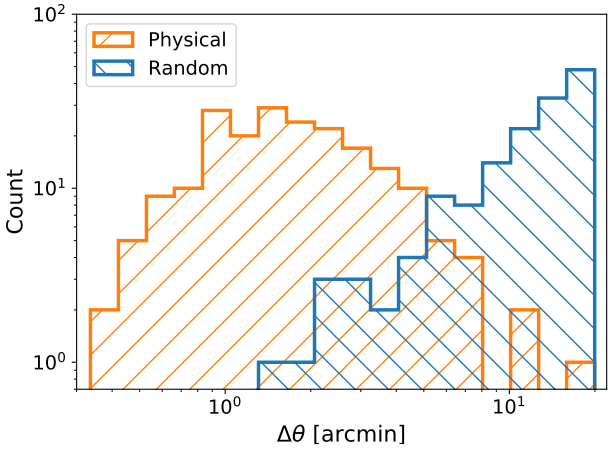


**Figure 2.** Histogram of the angular separation ($\Delta\theta$, in units of arcminutes) of random (blue) and physical (orange) pairs. While the random pairs are typically found at larger angular separations, there is a significant overlap for random and physical pairs in the range of $\Delta\theta$ from 2 to 10 arcmin.

## 3 RESULTS

In Fig. 2, we show the histogram of angular separations ($\Delta\theta$) for our sample of 148 random pairs (RPs) and 201 physical pairs (PPs). In both cases, we limited the maximum angular separation to 20 ar-

**Table 1.** Summary of results in the RM difference (ΔRM) between pairs.

| Classification | $N$ | $\Delta RM_{rms}$ rad m$^{-2}$ | $\Delta RM_{rms*}$ rad m$^{-2}$ | $\lvert\Delta RM\rvert_{median}$ rad m$^{-2}$ |
|---|---|---|---|---|
| Random pairs (RP) | 148 | 6.0±0.5 | 5.5±0.4 | 1.5±0.6 |
| Physical pairs (PP) | 201 | 1.4±0.1 | 1.4±0.1 | 0.7±0.1 |
| RP: 2 to 10 arcmin | 42 | 5.1±0.8 | 1.8±0.3 | 1.2±0.3 |
| PP: 2 to 10 arcmin | 75 | 1.4±0.2 | 1.4±0.2 | 0.9±0.2 |

$\Delta RM_{rms*}$: Trimmed rms, with one outlier from the random pairs removed.

cmin, with the RPs extending down to ∼1.5 arcmin and the PPs limited to the lower cut-off of 0.33 arcmin (i.e. the angular resolution). The limit of 20 arcmin was chosen because there are very few PPs above this separation. There is a clear difference in that the PPs are more often found at smaller angular separations (mean of 2 arcmin) than the random pairs (mean of 12 arcmin). This is expected since the PPs are limited to the linear size of the radio source, while the RPs have no such restriction. Since we want to compare the RPs and PPs, we are mainly interested in the region of significant overlap in angular separation between the two samples (in order to account for the Milky Way contribution). The overlap region we define here is from ∼2 to ∼10 arcmin, with 42 RPs and 75 PPs in this region (Table 1). For context, V19 found 317 PPs and 5111 RPs on angular scales from 1.5 to 20'. They chose an overlap region of 3 to 11 arcmin, which contained 158 RPs and 208 PPs. Although V19 had significantly more sources, our measurement errors are much lower, such that both experiments have comparable statistical power. The individual RM values for each pair are provided in Table 2.

Fig. 3 shows the individual values of $(\Delta RM)^2$ and $\Delta\theta$ for each source pair, with the RPs indicated by plus symbols and the PPs indicated by cross symbols. The mean RM error for our sample is 0.026 rad m$^{-2}$, and has a small contribution to the overall variance. The variance added by the measurement errors (i.e. $\sigma^2_{RM,err}$ in Eqn. 2) for physical and random pairs as a function of angular size is approximately constant, and shown in Fig. 3 as dashed and dot-dashed lines with values of ∼0.0018 rad$^2$ m$^{-4}$.

The root-mean-square of the RM difference for all RPs, $\Delta RM_{rms,RP} = 6.0 \pm 0.5$ rad m$^{-2}$ while $\Delta RM_{rms,PP} = 1.4 \pm 0.1$ rad m$^{-2}$ (in all cases we quote the rms with the error variance subtracted, and the associated uncertainty is the standard error in the mean). Kolmogorov-Smirnov (KS) and Anderson-Darling (AD) tests indicate that the difference between RPs and PPs is significant at $> 5\sigma$ (with p-values of $\sim10^{-7}$ and $\sim10^{-4}$ respectively). The empirical cumulative distribution function (ECDF) of $(\Delta RM)^2$ is shown in Fig. 4, with all PPs and RPs shown with dotted lines. This difference is dominated by the general trend of larger ΔRM variations at larger angular separations (Fig. 3), as is expected if the Milky Way ISM is the dominant contributing factor to the RM variance on these angular scales (e.g. Stil et al. 2011).

If we restrict the comparison only to the region of significant overlap in angular separation (i.e. 2 to 10 arcmin), then we have $\Delta RM_{rms,RP} = 5.1 \pm 0.8$ rad m$^{-2}$ and $\Delta RM_{rms,PP} = 1.4 \pm 0.1$ rad m$^{-2}$. However, the rms for the RPs is strongly affected by one outlier, with the highest value of $\Delta RM_{rms}$ in the sample of ∼954 rad$^2$ m$^{-4}$ (highlighted by a box in Fig 3). Therefore, we introduce the "trimmed rms" ($\Delta RM_{rms*}$) with this outlier removed. This reduces the rms of the RPs to $\Delta RM_{rms,RP} = 1.8 \pm 0.3$ rad m$^{-2}$, giving a difference of 0.4±0.3 rad m$^{-2}$ between the RPs and PPs between 2 and 10 arcmin. These results are summarised in Table 1, along with the median values of |ΔRM|. Similarly, there is a large difference in the median |ΔRM| values for all RPs and PPs of ∼0.8 rad m$^{-2}$, but a smaller difference of $0.3 \pm 0.4$ rad m$^{-2}$ between RPs and PPs in the overlap region. For the uncertainty in the median values (Williams 2001), we use standard error in the median (i.e. $\sqrt{\pi/2}$ times the standard error in the mean). KS and AD tests indicate that the RPs and PPs in the overlap region are not significantly different for these sample sizes (p-values of 0.17 and 0.06, respectively). The exclusion of the outlier does not significantly affect the KS or AD test results (p-values of 0.20 and 0.08). The ECDFs of $(\Delta RM)^2$ for only those RPs and PPs in the overlapping angular separation region of 2 to 10 arcmin are shown with solid lines in Fig. 4.

We also fit a power-law function to the RPs and PPs data, $(\Delta RM)^2 = k\,\Delta\theta^{\gamma}$, where $k$ is a constant with units of rad$^2$ m$^{-4}$ arcmin$^{-\gamma}$. We find $k_{RP} = 0.6 \pm 1.0$, $\gamma_{RP} = 0.6 \pm 0.4$ and

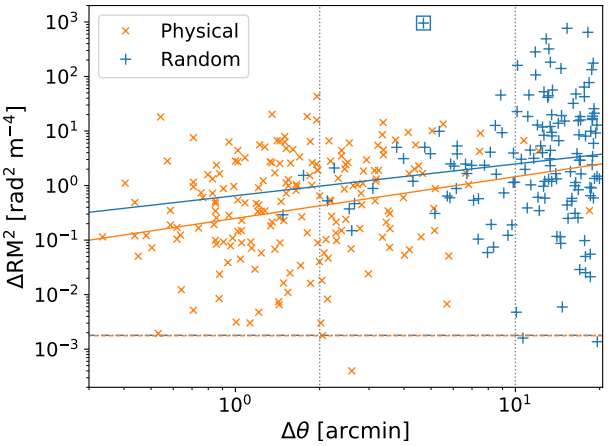


**Figure 3.** Scatter plot of the squared difference in RM, $(\Delta RM)^2$ in units of rad$^2$ m$^{-4}$, between pairs of radio sources versus the angular separation ($\Delta\theta$, in units of arcminutes). Physical pairs are shown as orange cross symbols while the random pairs are shown as blue plus symbols (with the outlier highlighted by a box). Power-law fits to the physical and random pair data are shown as solid orange and blue lines, respectively. The small, constant contributions to $(\Delta RM)^2$ from the measurement errors are shown for physical and random pairs as horizontal orange dashed and blue dot-dashed lines, respectively. The gray dotted vertical lines bound the overlap region of 2 to 10 arcmin.

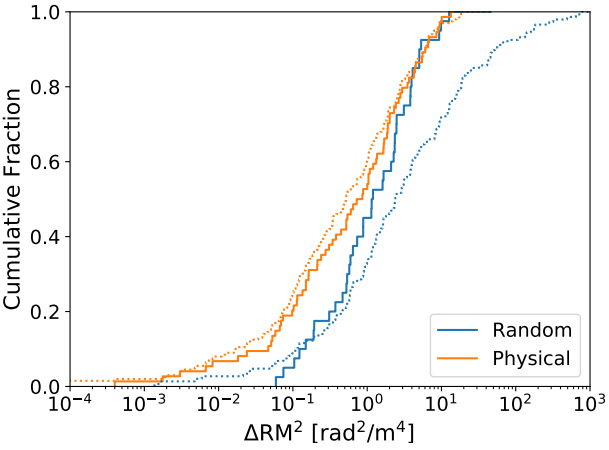


**Figure 4.** Empirical cumulative distribution functions (ECDFs) of the squared difference in RM, $(\Delta RM)^2$ in units of rad$^2$ m$^{-4}$, between pairs of radio sources. The dashed blue and orange lines correspond to all the data for physical and random pairs, respectively, while the solid blue and orange lines show only the corresponding data for physical and random pairs in the overlapping region of angular separation from 2 to 10 arcmin.

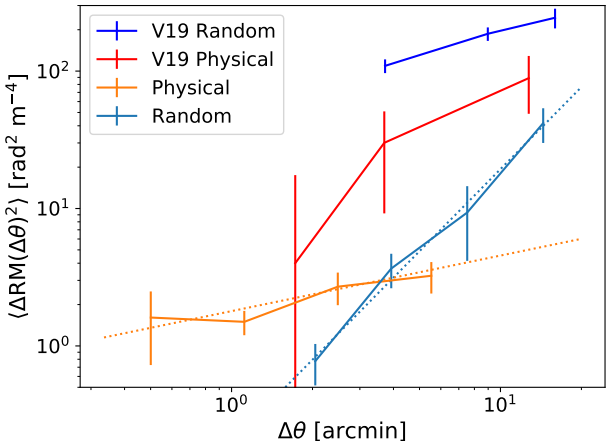


**Figure 5.** Plot of the RM structure functions (i.e. mean bins of $(\Delta RM)^2$ as a function of the pair angular separation, $\Delta\theta$) with the noise power from measurement errors subtracted, for PPs (orange) and RPs (blue). The orange and blue dotted lines show the power-law fits to the PPs and RPs, respectively. The RPs bin at the smallest angular separation has only 7 data points, and may be unreliable. For comparison, we also include the structure function results from the 1.4 GHz data of Vernstrom et al. (2019) for PPs (red) and RPs (dark blue).

$k_{\rm PP} = 0.25 \pm 0.04$, $\gamma_{\rm PP} = 0.8 \pm 0.2$. These fits are shown in Fig. 3. The difference in $(\Delta RM)^2$ between the power-law fits at the average separation in the overlapping region (i.e. 6') is $\sim$0.8 rad$^2$ m$^{-4}$. This is larger than the values estimated from the rms and median differences between RPs and PPs from 2 to 10 arcmin, which is not unexpected given that the fits are obtained using all the data. Attempts at fitting only the data in the overlapping region were poorly constrained, so we do not include them here.

To more directly compare with the results of V19, we calculate the mean of $(\Delta RM)^2$ as a function of the angular separation, i.e. the RM structure function (SF), with

$$\langle \Delta {\rm RM}(\Delta\theta)^2 \rangle = \frac{1}{N} \sum_i [{\rm RM}_1(\theta) - {\rm RM}_2(\theta + \Delta\theta)]_i^2 \,. \qquad (5)$$

This is done separately for the RPs and PPs, and they are plotted in Fig. 5 in addition to the V19 RM structure functions. By fitting power-laws to these data in a similar manner to above, with $\langle(\Delta RM)^2\rangle = k_{\rm SF}\,\Delta\theta^{\gamma_{\rm SF}}$, we find $k_{\rm SF,RP} = 0.2 \pm 0.1$, $\gamma_{\rm SF,RP} = 1.9 \pm 0.2$ (with the outlier removed) and $k_{\rm SF,PP} = 1.8 \pm 0.3$, $\gamma_{\rm SF,PP} = 0.4 \pm 0.1$. These fits are shown by dotted lines in Fig. 5. The values of $\gamma_{\rm SF}$ are in stark contrast with those found in V19 ($\gamma_{\rm SF,RP,NVSS} = 0.6 \pm 0.1$, $\gamma_{\rm SF,PP,NVSS} = 0.8 \pm 0.2$) with the RPs slope being much steeper than in V19 and the PPs slope being much flatter. Also notable is that the overall amplitude is smaller in both cases compared to V19 ($k_{\rm SF,RP,NVSS} = 50 \pm 30$, $k_{\rm SF,PP,NVSS} = 11 \pm 15$). These differences have important implications for the nature of the extragalactic Faraday rotating material and are addressed in the next section.

### 3.1 Comparison with RM data at 1.4 GHz

We find that 203 out of the 698 source components in this study ($\sim$29%) have corresponding RM values at 1.4 GHz in the Taylor et al. (2009) catalog. The vast majority, 91% (97%), of the corresponding RM values are consistent within $3\sigma$ ($5\sigma$) of the combined RM error. The LOFAR sources that are not in the NVSS RM catalog are on average $\sim$3 times fainter in total intensity at 150 MHz. This means that the majority of the LOFAR polarized sources are too faint to be detected in the NVSS. For those pairs that have counterparts in the V19 catalog, we find $\Delta{\rm RM}_{\rm rms,RP,NVSS} \sim 18$ rad m$^{-2}$ and $\Delta{\rm RM}_{\rm rms,PP,NVSS} \sim 5$ rad m$^{-2}$, which is consistent with the results presented in V19. However, for the exact same sources we find $\Delta{\rm RM}_{\rm rms,RP,LOFAR} \sim 5$ rad m$^{-2}$ and $\Delta{\rm RM}_{\rm rms,PP,LOFAR} \sim 2$ rad m$^{-2}$.

For the RPs, the large difference in the RM variance properties of these sources between 1.4 GHz and 150 MHz is most likely related to the broader range of Faraday depths that are probed local to the sources at 1.4 GHz (in terms of both the larger synthesised beam and the extent of the source polarization detected). It may also be the case that Faraday complexity is affecting the observed RM value at 1.4 GHz, as $\sim$40% of the RPs include a compact radio source. The smaller difference between the 1.4 GHz and 150 MHz data for PPs support this idea as more of the RM structure is resolved for the individual sources. However, more detailed investigation is needed with high angular resolution observations of these sources at 1.4 GHz to test this. In general, this indicates that the LOFAR observations are only sensitive to the low RM variance regions of these radio sources, and that the differences between the V19 results and those presented here are most likely related to the RM properties of the local source environment.

This hypothesis is further supported by direct comparison of the RM structure function values found in the previous section and shown in Fig. 5. The difference between the RP data at 1.4 GHz and 150 MHz is $\sim$7 rad m$^{-2}$, which is comparable to the total extragalactic RM variance estimated by V19, Schnitzeler (2010) and Oppermann et al. (2015). One possibility is that this may reflect the typical contribution to the RM variance at 1.4 GHz provided by the magnetized intracluster medium surrounding radio galaxies. In this case, the Faraday depolarization caused by small scale magnetic field fluctuations in these environments is sufficient to completely depolarize the emission at 150 MHz, thus removing the majority of these sources from the LOFAR sample.

Finally, the much steeper slope of the RM structure function for RPs (compared to V19, see Fig. 5) may more cleanly reflect the RM variance from the Milky Way on these angular scales, if the extragalactic RM variance contribution is indeed much lower for the LOFAR data (more data for the PPs at large angular separations are needed to test this hypothesis). In fact, the LOFAR data are more consistent with the model Milky Way RM structure function derived in Akahori et al. (2013), who used MHD simulations to model the RM variance contribution expected from the Milky Way towards high Galactic latitudes. This may also be related to the flattening of the slope of the RM structure function towards smaller angular scales (as probed by the PPs), reflecting the growing dominance of the extragalactic RM contribution, with $\langle(\Delta RM)^2\rangle \lesssim 1.6$ rad$^2$ m$^{-4}$ on the smallest angular separations (Fig. 5). We use this limit as a constraint for cosmological simulations in Section 4.2.

## 4 SIMULATIONS

### 4.1 Monte Carlo Modelling of Extragalactic RM Pairs

In order to understand the implications for the properties of intergalactic magnetic fields based on the results in Section 3, we develop some basic simulations of extragalactic Faraday rotation. We use models for the magnetic field and electron density of voids and filaments that are consistent with observational knowledge, in order to calculate the RM along different cosmic sight lines for RPs

and PPs with a range of angular separations. This model allows us to perform a complete survey of the strength and correlation length of magnetic fields in the intergalactic medium (IGM), constrained by the RM observations, albeit under a few simplifying assumptions on the distribution of free electrons, and on the existence of a single typical correlation scale of magnetic fields along the lines of sight probed by our observations of galaxies. Although simple, the model described below is a significant advance on models that consider only homogenous distributions of electron density and magnetic field along the line of sight, and can be developed further as our understanding of the observational facts improve (e.g. after obtaining the redshift distribution of the sources in our sample).

Following Blasi et al. (1999) and Pshirkov et al. (2016), we model the electron number density along cosmic lines of sight as $n_e(z) = n_e(0)(1+\delta_e)(1+z)^3$, with $n_e(0) = 1.8 \times 10^{-7}$ cm$^{-3}$ and $\delta_e$ being the electron overdensity. We draw the electron overdensity $\delta_e$ from a log-normal distribution, with $\delta_e$ varying on scales of the Jeans length, $\lambda_J(z) \sim 2.3(1+z)^{-1.5}$ Mpc. The log-normal distribution is given by

$$P(\delta_e) = \frac{1}{\sqrt{2\pi}\sigma_e(1+\delta_e)} \exp\left\{-\frac{[\ln(1+\delta_e) - \mu_e(z)]^2}{2\sigma_e^2}\right\}, \quad (6)$$

where the mean ($\mu_e$) and standard deviation ($\sigma_e$) of the logarithm of the $\delta_e$ distribution are constrained from observations of the Lyman-$\alpha$ forest (e.g. Bi & Davidsen 1997), with $\sigma_e(z) = 0.08 + 5.37(1+z)^{-1} - 4.21(1+z)^{-2} + 1.44(1+z)^{-3}$ and $\mu_e(z) = -\sigma_e(z)^2/2$. For close pairs of sources we also need to include a prescription for the correlation of the densities along adjacent lines of sight. For this we use the two-point galaxy correlation function $\xi(r,z) = (r/r_0)^{-\gamma}(1+z)^{-(2+\gamma)}$, including its expected redshift evolution, with $\gamma \sim 1.8$ and $r_0 \sim 5h^{-1}$ Mpc (e.g. Mo et al. 2010). We consider this correlation function valid for scales between $0.2h^{-1}$ to $30h^{-1}$ Mpc. Practically, we implement the correlated draws using a bi-variate Gaussian distribution before taking the exponential, where the off-diagonal terms of the covariance matrix are given by $\xi_G = \ln(1+\xi)$ (e.g. Coles & Jones 1991; Chuang et al. 2015; Baratta et al. 2019). For separations between adjacent cells larger than $30h^{-1}$ Mpc, we draw from an uncorrelated log-normal distribution, while the same density is assigned for cell separations less than $0.2h^{-1}$ Mpc.

We model the magnetic field strength as a scaled function of the density and redshift following $B(z) = B_0[n_e(z)/n_e(0)]^{2/3}$, which is a reasonable expectation in the case of isotropic gas compression in filaments of the cosmic web (e.g. Locatelli et al. 2018), In this case, we have $B_0$ as the co-moving cosmological magnetic field strength in nG. The correlation length of the magnetic field ($l_B$) is set in fractions of the Jeans length, with random orientations assigned at each step by multiplying the amplitude of the field by a number drawn from a uniform [−1, 1] distribution. The RM values were obtained by summing the RM contributions over all cells along an individual line of sight (from the source to us), while accounting for the RM redshift dilution of $(1+z)^2$ in each cell.

Since we do not know the redshift distribution of our sample, we randomly draw sources from a log-normal redshift distribution ($\mu_z = -1$, $\sigma_z = 1$), which has a median of $z \sim 0.37$ and is consistent with the redshift distribution of polarized extragalactic radio sources (Vernstrom et al. 2019; Hardcastle et al. 2019; O'Sullivan et al. 2018a). However, we limit the redshift to a maximum of 1 for the PPs and 4 for the RPs following the corresponding maximum redshifts found in V19. We note that the actual redshift distribution of the LOFAR data may be somewhat different because the sources are typically fainter in total intensity that those at 1.4 GHz (Section 3.1). Similarly, we do not know the projected linear size distribution of our physical pairs, but we can again reasonably model this as a log-normal distribution ($\mu_{\rm ls} = -1$, $\sigma_{\rm ls} = 1$) in Mpc units based on the projected linear size distributions for LOFAR radio galaxies in Hardcastle et al. (2019). For an angular size ranging from 2 to 10 arcmin, this gives a maximum linear size of ∼5 Mpc and a minimum of ∼24 kpc, which is consistent with the range of linear sizes of LOFAR polarized sources (O'Sullivan et al. 2018a). In general, this aspect of the analysis can be substantially improved when the redshifts of the LOFAR polarized sources become available in the upcoming LoTSS DR2 value-added catalog.

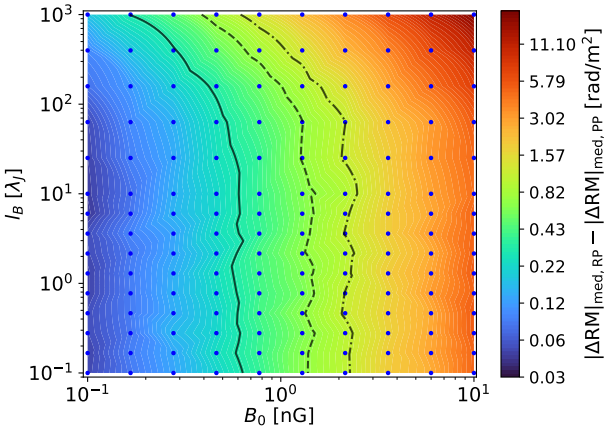


**Figure 6.** Based on the model described in Section 4.1, here we show the parameter space for the average extragalactic magnetic field strength ($B_0$ in nG) and correlation length ($l_B$ in dimensionless units of the Jeans length, $\lambda_J$). The value of $|\Delta RM|_{\rm median,RP} - |\Delta RM|_{\rm median,PP}$ is shown by the colour scale, which is linearly interpolated between the model output at the grid points (shown as dots). The solid black line shows the locus of the median difference in ΔRM between RPs and PPs for the observational data of 0.3 rad m$^{-2}$, with the dashed and dot-dash lines corresponding to one and two times the standard error in the median of ±0.4 rad m$^{-2}$. Thus, to the left of the dashed line provides a limit on the average extragalactic magnetic field strength of $B_0 < 2.5$ nG for magnetic field correlation lengths in the range $0.1 \leq l_B/\lambda_J \leq 1000$.

For the PPs, we first draw the redshift of the radio galaxy. Then we draw the linear size from the linear size distribution and compute the separation, $\theta$, between the pair using the angular diameter distance. We construct two sight lines to the radio galaxy, only allowing the range $2 < \theta < 10$ arcmin, to obtain the RM for each sight line, before calculating the RM difference (in a random manner). For the RPs, we draw a redshift for each radio galaxy, with a fixed $\theta$ of 6 arcmin (i.e. the mean observational separation for the RPs in the overlap region), before calculating the RM difference. To create distributions of ΔRM, we calculate the RM difference for 10,000 draws each for both RPs and PPs. This produced smooth distributions of ΔRM from which we could obtain reliable statistics.

We then generate ΔRM distributions for RPs and PPs for a grid of $B_0$ and $l_B$ values. The simulations are run for a grid of $0.1 \leq B_0 \leq 10$ nG and $0.1 \leq l_B/\lambda_J \leq 10$, both with 10 even steps in log space. To extend the grid to large values of $l_B$, we also produce ΔRM distributions for $10 \leq l_B/\lambda_J \leq 1000$ in 5 even steps in log space (i.e. for a total of 150 grid points). We employ a parallelized version of the code (using the joblib python library[4]), which takes

[4] https://joblib.readthedocs.io/en/latest/parallel.html

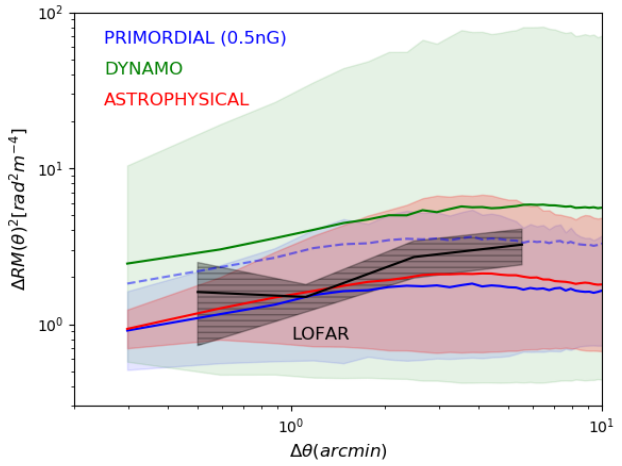


**Figure 7.** Simulated distribution of $\Delta\mathrm{RM}(\Delta\theta)^2$ as a function of angular separation for three numerical models, as described in Section 4.2, compared with LOFAR data. The solid lines show the mean values and the shaded region shows the $1\sigma$ dispersion. The dark shaded region outlining the LOFAR data is identical to that shown in Fig. 5 for the PPs. The dashed blue line give the prediction for a uniform primordial model using $B_0 = 1$ nG (comoving), while the solid blue line is the result of post-processing by rescaling it to $B_0 = 0.5$ nG (comoving). The variance around each model is due to the redshift distribution of sources.

approximately 3 weeks to run on 24 cores. The median of $|\Delta\mathrm{RM}|$ was chosen as the most robust statistic for comparison with the observational data (see Table 1). This is because the mean $(\Delta\mathrm{RM})^2$ values from the model are strongly affected by outliers, due to the lognormal density distribution (e.g. Blasi et al. 1999).

Figure 6 shows the value of $|\Delta\mathrm{RM}|_{\mathrm{median,RP}} - |\Delta\mathrm{RM}|_{\mathrm{median,PP}}$ for variations in $B_0$ and $l_B$. The solid, dashed and dot-dash lines correspond to the observed median difference of 0.3 rad m$^{-2}$, and one and two times the standard error in the median, respectively. We consider the region to the left of the dot-dashed contour of 1.1 rad m$^{-2}$ as consistent with the data (i.e. the observed difference of 0.3 rad m$^{-2}$ plus twice value of the standard error in the median of 0.4 rad m$^{-2}$). Therefore, this places a conservative limit on the co-moving cosmological magnetic field of $B_0 < 2.5$ nG for correlation lengths ranging from $0.1 \leq l_B/\lambda_J \leq 1000$. This limit should not be confused with the magnetic field strength in filaments which can often be up to 20 times larger in this model. We note that the individual $|\Delta\mathrm{RM}|_{\mathrm{median}}$ values for RPs and PPs from the simulation for $B_0 < 2.5$ nG do not exceed the corresponding observational values in Table 1. This is expected because the individual observational values are still contaminated by the Milky Way contribution (which is absent from the model). This provides further evidence for the robustness of this simple model of extragalactic magnetic fields.

### 4.2 Comparison with cosmological simulations

For an alternative constraint, we use the results of recent magneto-hydrodynamical (MHD) simulations considering several different scenarios for the origin and amplification of extragalactic magnetic fields (Vazza et al. 2017). The comparison that we focus on in this case is with the LOFAR RM structure function for the PPs on small angular scales (c.f. Fig. 5 for $\Delta\theta < 1$ arcmin). We consider this the most relevant constraint because the extragalactic contribution to the structure function may begin to dominate at small angular scales since the contribution of the Milky Way ISM is expected to decline steeply with decreasing angular scale (e.g. Akahori et al. 2013, 2014). In contrast to the model described in Section 4.1, here the 3-dimensional distribution of magnetic fields and electron density in the cosmic volume are self-consistently produced by the MHD simulation, depending on different assumed scenarios for magnetogenesis. Here we focus on three of the most realistic scenarios, within a larger survey of 25 models presented in Vazza et al. (2017). A detailed survey of all models allowed by the LOFAR data is beyond the scope of the current work, but will become more feasible when we know the redshift distribution of the LOFAR sources.

The three different scenarios were simulated in a comoving $(85\ \mathrm{Mpc})^3$ volume with $1024^3$ cells, using the ENZO code (Vazza et al. 2017). The different prescriptions for the injection and evolution of magnetic fields were: a) a primordial, uniform, volume-filling, comoving magnetic field of $B_0 = 1$ nG at the beginning of the simulation; b) a primordial model starting from the much lower level of $B_0 = 10^{-9}$ nG but including a run-time modelling of dynamo amplification of the magnetic field; c) an "astrophysical" run in which the magnetic field is injected solely by feedback events from star forming regions and/or active galactic nuclei. For scenario a), a residual level of magnetization (~1 to 10 nG) is present everywhere in the cosmic volume. However, in scenarios b) and c) the average magnetization is a steeper function of density. Particularly in the astrophysical scenario, very little magnetic fields are present outside of the virial volume of matter halos, due to the strong association between sources of magnetization and the halos. For more details we refer the reader to Vazza et al. (2017) and Gheller & Vazza (2019).

In order to construct synthetic RM structure functions for the PPs for each magnetogenesis scenario, simulated maps of Faraday rotation for a 4° field of view were created, before obtaining deep lightcones by stacking different snapshots along the line of sight. We note that the generation of synthetic RM structure functions for RPs was beyond the scope of the current work, but will be investigated in a future publication. In detail, using different snapshots of the above runs, we integrated along lightcones up to $z = 0.5$, and simulated $(\Delta\mathrm{RM})^2$ for PPs, by placing pairs of sources at regular intervals of 85 Mpc (co-moving) along the line of sight (i.e. at the end of each of the co-moving volumes used to produce the stacked sequence of Faraday rotation). Note that the pairs are not located at the physical location of the AGN outflows. We first randomly drew 1500 sources, with $|\mathrm{RM}| \geq 0.03$ rad m$^{-2}$, for 22 evenly spaced redshift bins. We then computed the $\Delta\mathrm{RM}(\Delta\theta)^2$ statistics at each redshift, and finally produced the observable total distribution of $\Delta\mathrm{RM}(\Delta\theta)^2$ by weighting each structure function by the distribution function of source redshifts approximately derived from V19. Considering the constant spatial resolution of the cosmological simulations (83 kpc/cell), we note that scales below 1 arcmin are not resolved by the simulation for the $z \leq 0.07$ portion of the lightcone. While this effect is small, considering that little magnetic structure is expected below 100 kpc in the low density part of the cosmic web (e.g. Vazza et al. 2015), this likely makes our simulated distribution of $(\Delta\mathrm{RM})^2$ for $\Delta\theta \leq 1$ arcmin a *lower limit* of the true distribution that can be expected for each model.

Figure 7 shows the simulated distribution of $\Delta\mathrm{RM}(\Delta\theta)^2$ as a function of angular separation for the three models, enabling a direct comparison with the LOFAR data (dark shaded region). Note that the RM variance from the Milky Way is not included in the

models (so the model trends are not expected to exceed the LOFAR curve). Both the uniform primordial model (blue dashed line) and the dynamo amplification model (green) are inconsistent with the LOFAR observations. Based on the typical range of magnetic field measured within filaments in these runs (Gheller & Vazza 2019, fig. 6), this suggests a limit of $\lesssim$ 10 to 100 nG on the average magnetization of filaments crossed by the polarized emission observed with LOFAR. On the other hand, the astrophysical scenario (red line) gives a more reasonable agreement with the LOFAR data, which follows from the fact that in this case the magnetic fields in filaments are far less volume filling, with a broad distribution of values centred around $\sim$ 1 nG. Considering the present data, we note that a simple rescaling of the uniform primordial field by a factor of $\sim$ 1/2 produces a similar result as in the astrophysical scenario. This in turn suggests that $B_0 \approx 0.5$ nG is the new limit on the strength of primordial magnetic fields that can be inferred from the LOFAR data (at least in the simple case of a spatially uniform seed magnetic field). Conversely, no rescaling can reconcile the simulated statistics of $\Delta\mathrm{RM}(\Delta\theta)^2$ in the dynamo case, because the observed scatter in the LOFAR observations is more than one order of magnitude smaller than what is produced by the large fluctuations that are present across the distribution of filaments in the dynamo scenario (e.g. Ryu et al. 2008).

## 5 DISCUSSION

The goal of this work is to isolate the extragalactic RM variance from the other contributions along the line of sight (e.g. Eqn. 2). The RM variance introduced by the ionosphere ($\sigma^2_{\mathrm{RM,ion}}$) was accounted for by restricting the RM difference of close pairs of radio sources, $(\Delta\mathrm{RM})^2$, to come from the same observational pointing, in addition to the standard correction of the time-variable ionosphere RM as described in Section 2. The RM variance contributed by measurement errors ($\sigma^2_{\mathrm{RM,err}}$) was subtracted from the quoted rms values, although the effect of this is minor due to the small LOFAR RM errors ($\sim 0.03$ rad m$^{-2}$). We then split the $(\Delta\mathrm{RM})^2$ sample into pairs from the same physical source (physical pairs; PPs) and non-physical, random pairs on the sky (random pairs; RPs). The comparison of these two samples can then be used to account for the Milky Way contribution ($\sigma^2_{\mathrm{RM,MW}}$) in a statistical sense. In principle, this leaves only the contribution from extragalactic Faraday rotation. By analysing the difference in $(\Delta\mathrm{RM})^2$ between RPs and PPs in three different ways (rms, median & power-law fits) in Section 3, we find that the extragalactic RM variance ($\sigma^2_{\mathrm{RM,ex}}$) of our LOFAR data is $\lesssim 1$ rad$^2$ m$^{-4}$. In particular, we focus on the trimmed rms difference between RPs and PPs of $0.4 \pm 0.3$ rad m$^{-2}$ and the median difference of $0.3 \pm 0.4$ rad m$^{-2}$, with both obtained in the range of angular scales with appreciable overlap (i.e. 2 to 10 arcmin).

### 5.1 The Faraday medium local to radio sources

For the purpose of this discussion, we further split the extragalactic RM variance into contributions local to the sources ($\sigma^2_{\mathrm{RM,local}}$) and from the intergalactic medium in filaments and voids on large scales ($\sigma^2_{\mathrm{RM,IGMF}}$). At 1.4 GHz, V19 found an rms difference of $\sim$5 to 10 rad m$^{-2}$ between RPs and PPs. This is similar to $\sigma_{\mathrm{RM,ex}} \sim 7$ rad m$^{-2}$ estimated by Schnitzeler (2010) and Oppermann et al. (2015) at 1.4 GHz. However, our result at 150 MHz appears to be in large conflict with the 1.4 GHz results, as one does not expect a frequency-dependent RM contribution from magnetic fields in voids and filaments. Instead, what our results strongly suggest is that the rms difference of $\sim$5 to 10 rad m$^{-2}$ found in V19 between RPs and PPs is dominated by RM variance local to the source (i.e. from $\sigma^2_{\mathrm{RM,local}}$).

Indeed, V19 estimate that the average difference in local density or magnetic field strength in RPs needs to be only a factor of $\sim$1.7 larger than the average difference in density or magnetic field strength between PPs. For our LOFAR data, there must be a much smaller variation in the magnetoionic properties between RPs and PPs. Assuming a redshift distribution similar to that in V19, then the difference in magnetoionic properties between RPs is at most 15% larger than in PPs. Therefore, the difference between our results and V19 is not only about the higher RM precision provided by LOFAR but also points towards a significantly different population (or sub-population) of polarized radio sources being probed at 150 MHz (see Section 3.1).

For example, for a polarized signal to be detected at 150 MHz, only small amounts of Faraday depolarization within the LOFAR synthesised beam are possible (e.g. less than 0.4 rad m$^{-2}$ on scales $<$ 20 arcsec for the most common model of external Faraday dispersion, Burn (1966), with $p(\lambda) \propto e^{-2\sigma^2_{\mathrm{RM}}\lambda^4}$). Alternatively, the polarized signal may originate from a compact emission region on sub-beam scales (e.g. hotspots), and thus the inferred Faraday depolarization would not represent the RM variance on larger scales (i.e. as would be relevant for physical pairs on scales $>$ 100 kpc). In any case, for radio sources in regions of dense magnetized gas, such as near the centre of groups and clusters of galaxies, there is likely too much Faraday depolarization for emission to be detected at 150 MHz. Furthermore, large asymmetries in the Faraday rotation properties of opposite lobes are often found in these rich environments due to, for example, the Laing-Garrington effect (Laing 1988; Garrington et al. 1988), which would make the detection of polarized emission from physical pairs less likely compared to physically large radio sources that are closer to the plane of the sky (e.g. Saripalli & Subrahmanyan 2009). This is consistent with recent results that find the majority of polarized detections in LOFAR data are from hotspots of FRII radio galaxies that are not associated with galaxy clusters and have large physical sizes (O'Sullivan et al. 2018a; Stuardi et al. 2020; Mahatma et al. 2020). Therefore, we expect that LOFAR polarized sources are typically located in regions of the Universe with low RM variance. This makes them ideal probes of the weak magnetization of the cosmic filaments and voids far from galaxy cluster environments.

### 5.2 Model limits on intergalactic magnetic fields

In Section 4, we take two approaches to deriving upper limits on intergalactic magnetic fields in filaments and voids. In one approach, we use a Monte Carlo model to generate distributions of $\Delta$RM for RPs and PPs in a universe with an inhomogeneous matter distribution and with a magnetic field which is a function of the density inhomogeneities (i.e. $B \propto n_e^{2/3}$). The model allows us to explore a wide range of input co-moving cosmological magnetic field strengths ($0.1 \leq B_0 \leq 10$ nG) and correlations lengths ($0.1 \leq l_B/\lambda_J \leq 1000$). For this model, we find that the median $|\Delta\mathrm{RM}|$ is the best statistical indicator due to the highly non-Gaussian $\Delta$RM distribution. Using the observational constraint of the difference in the median $|\Delta\mathrm{RM}|$ between RPs and PPs of $0.3 \pm 0.4$ rad m$^{-2}$ provides a upper limit of $B_0 < 2.5$ nG for magnetic field correlation lengths $l_B/\lambda_J \leq 1000$ (where $\lambda_J \sim 2.3$ Mpc at $z = 0$). This limit is comparable with upper limits on the primordial field from CMB measurements (Planck Collaboration et al. 2016a), and more than an order

of magnitude better than the upper limit of ∼37 nG on the strength of the IGMF derived in V19 (for a homogenous universe with $n_e$ of $10^{-5}$ cm$^{-3}$ and a magnetic field correlation length of 1 Mpc).

In the second approach, we compare our observational results with cosmological MHD simulations (Vazza et al. 2017) in three different scenarios: a) a primordial field of $B_0 = 1$ nG, b) a primordial field of $B_0 = 10^{-9}$ nG with dynamo amplification, and c) magnetization only from AGN and galactic outflows. In this approach, the most useful constraint comes from the RM structure function on the smallest angular scales because this should have the smallest contribution from the RM variance of the Milky Way (which is not included in the models). In particular, synthetic RM structure functions for PPs were created from the simulations (as described in Section 4.2) and constrained by the data for angular separations less than 1 arcmin (i.e. $\langle(\Delta\mathrm{RM})^2\rangle < 1.6$ rad$^2$ m$^{-4}$). Both the scenario of magnetization by astrophysical processes (e.g. AGN and galactic outflows) and the primordial case are consistent with the data, once the primordial field is scaled to a smaller initial (spatially uniform) seed field of $B_0 \lesssim 0.5$ nG. The dynamo amplification scenario is inconsistent with the data as it produces ΔRM fluctuations that are too large. These inferences can be considered preliminary, since one of the main limitations of the comparison between the models and the data is our lack of knowledge of the exact redshift distribution of the observed radio sources. For example, we do not know the true distribution of physical (and angular) separations for PPs as a function of redshift. Furthermore, we have not included a cosmological model for the RPs, again due to redshift uncertainty. For future work, in addition to more realistic models based on observed redshifts, we plan to explore how the LOFAR data might also constrain the morphology of primordial magnetic fields, whose initial spectra are already constrained by PLANCK observations (Planck Collaboration et al. 2016a). In general, this highlights the potential of LOFAR data to realistically discriminate between competing magnetogenesis scenarios.

### 5.3 Upcoming advances

Much more can be achieved in the near future with LOFAR. In particular, we expect the sample of pairs to potentially increase by an order of magnitude for the full LoTSS survey, helping to push well into the sub-nG regime for the study of cosmic magnetic fields. In the near term, host galaxy identifications and redshifts will be provided by the value-added data products in LoTSS DR2. We expect to get photometric or spectroscopic redshifts for ∼80% of the polarized sources in our current sample (O'Sullivan et al. 2018a). With the LOFAR-WEAVE survey (Smith et al. 2016), we expect spectroscopic redshifts for all the polarized radio sources in LoTSS up to at least $z = 1$. In combination with the high-fidelity 6 arcsec total intensity images provided by the LoTSS survey, these redshifts will enable precise linear size estimates of the sources, which will further enhance our ability to distinguish between magnetoionic material local to the source and that associated with cosmic filaments and voids. In addition, splitting the sample into redshift bins (in addition to $\Delta z$ bins for the random pairs) will allow investigations of the evolution of magnetic fields with cosmic time.

In order to learn more about the properties of LOFAR polarized sources (and the IGMF), we will need to consider several other properties, such as the degree of polarization/depolarization, the total intensity spectral index, the radio source morphology, the environment, etc. Such investigations are important to allow a better understanding of the different astrophysical contributions to the total observed RM variance, to weight the RM variance of each sub-population in an appropriate manner (e.g. Rudnick 2019), and to potentially remove blazars from the sample. This should be done in combination with other upcoming RM surveys at higher frequencies (e.g. POSSUM, VLASS; Gaensler et al. 2010; Lacy et al. 2019), which can probe cosmic magnetic fields in high density environments that are currently inaccessible for LOFAR. In the longer term, both the SKA-Low and SKA-Mid (e.g. Braun et al. 2015, and references therein) will be essential to further map out the frequency-dependent behaviour of the extragalactic RM variance in order to uncover the nature of magnetic fields in the cosmic web.

## 6 CONCLUSIONS

We have presented a Faraday rotation study of 349 close pairs of extragalactic radio sources with LOFAR, to investigate the properties of extragalactic magnetic fields. The data used are from the ongoing LOFAR Two-Metre Sky Survey (LoTSS; Shimwell et al. 2019), which is imaging the northern sky in continuum polarization from 120 to 168 MHz. The large bandwidth at such low frequencies provides exceptional RM precision, with typical errors of ∼0.03 rad m$^{-2}$, which is ∼ 300 times better than in the previous best study (Vernstrom et al. 2019). By considering the variance of the RM difference between physical pairs (e.g. double-lobed radio galaxies) and random pairs (i.e. physically different sources with close projected separations on the sky), we can statistically separate the extragalactic component of the RM variance from that due to the Milky Way. In the region of overlapping angular scales from 2 to 10 arcmin, we find a trimmed rms RM difference of 1.8 ± 0.3 rad m$^{-2}$ for 41 random pairs and 1.4±0.2 rad m$^{-2}$ for 75 physical pairs, providing an estimate for the extragalactic rms RM contribution of 0.4 ± 0.3 rad m$^{-2}$. A similar estimate of 0.3 ± 0.4 rad m$^{-2}$ is provided by analysis of the median |ΔRM|. This shows that LOFAR polarized sources probe regions of low extragalactic RM variance.

This result is in apparent conflict with estimates of the extragalactic variance of ∼5 rad m$^{-2}$ derived from observations at 1.4 GHz (Vernstrom et al. 2019). There is no expectation of a frequency-dependent RM from magnetic fields in cosmic filaments and voids. Therefore, our results point to the contribution of magnetoionic material local to the radio source as the dominant extragalactic contribution at 1.4 GHz (e.g. the magnetized IGM of galaxy groups and clusters). This means that sources in Vernstrom et al. (2019) with large RM variance local to the source are depolarized below the detection limit at 150 MHz. With these sources missing from the LOFAR sample, our data are probing the low RM variance Universe, providing even more stringent constraints on the magnetization of the cosmic web away from galaxy cluster environments.

To investigate the implication of our results for the strength of magnetic fields in filaments and voids, we develop a model to calculate the RM difference between adjacent pairs of cosmic sight-lines. The model accurately reflects real cosmic over-densities, including the expected density correlation for close pairs, and describes a 'frozen-in' magnetic field that scales with the density. We use this model to generate ΔRM distributions for random and physical pairs in the cases of co-moving cosmological magnetic fields strengths ($B_0$) ranging from 0.1 to 10 nG. We find that the difference in the median |ΔRM| provides the most robust statistical constraint. This allows us to place a conservative limit of $B_0 < 2.5$ nG for magnetic field correlations lengths between ∼0.1 and 1000 Mpc.

We also compare our results with a suite of cosmological MHD simulations, allowing us to investigate some different mag-

netogenesis scenarios. In particular, we investigated the RM variance generated in three different scenarios: a strong initial primordial field of 1 nG, a weak primordial field of $10^{-9}$ nG but with dynamo amplification, and an astrophysical scenario where magnetic field is injected by AGN and galactic outflows. To constrain the different simulation scenarios, we use the RM structure function of physical pairs on angular scales less than 1 arcmin. We do this because these data should have the lowest RM variance contribution from the Milky Way (which is not included in the model). We find that both the astrophysical scenario and a primordial scenario with a weaker seed field of $B \lesssim 0.5$ nG are consistent with the current data. Interestingly, the dynamo amplification scenario is disfavoured because the dispersion in RM is much larger than the observed scatter in the LOFAR data.

In the coming years, we will be able to significantly expand on the current sample, in addition to adding redshift information for the host galaxies of the radio sources. This will allow us to push well into the sub-nG regime and further constrain both the origin and evolution of cosmic magnetic fields on large scales.

## ACKNOWLEDGMENTS

SPO and MB acknowledge financial support from the Deutsche Forschungsgemeinschaft (DFG) under grant BR2026/23. MB acknowledges support from the Deutsche Forschungsgemeinschaft under Germany's Excellence Strategy - EXC 2121 "Quantum Universe" - 390833306. FV and NL acknowledge financial support from the Horizon 2020 programme under the ERC Starting Grant "MAGCOW", no. 714196. The ENZO (enzo-project.org) simulations used for this work were produced on the CSCS Supercomputer of ETHZ (Lugano) and on the Marconi Supercomputer at CINECA (Bologna), under project no. INA17_C4A28 with FV as PI. FV gratefully acknowledge the usage of online storage tools kindly provided by the INAF Astronomical Archive (IA2) initiative (http://www.ia2.inaf.it). LOFAR (van Haarlem et al. 2013) is the Low Frequency Array designed and constructed by ASTRON. It has observing, data processing, and data storage facilities in several countries, that are owned by various parties (each with their own funding sources), and that are collectively operated by the ILT foundation under a joint scientific policy. The ILT resources have benefitted from the following recent major funding sources: CNRS-INSU, Observatoire de Paris and Université d'Orléans, France; BMBF, MIWF-NRW, MPG, Germany; Science Foundation Ireland (SFI), Department of Business, Enterprise and Innovation (DBEI), Ireland; NWO, The Netherlands; The Science and Technology Facilities Council, UK; Ministry of Science and Higher Education, Poland. Part of this work was carried out on the Dutch national e-infrastructure with the support of the SURF Cooperative through grant e-infra 160022 & 160152. The LOFAR software and dedicated reduction packages on https://github.com/apmechev/GRID_LRT were deployed on the e-infrastructure by the LOFAR e-infragroup, consisting of J. B. R. Oonk (ASTRON & Leiden Observatory), A. P. Mechev (Leiden Observatory) and T. Shimwell (ASTRON) with support from N. Danezi (SURFsara) and C. Schrijvers (SURFsara). This research has made use of data analysed using the University of Hertfordshire high-performance computing facility (http://uhhpc.herts.ac.uk/) and the LOFAR-UK computing facility located at the University of Hertfordshire and supported by STFC [ST/P000096/1]. SPO thanks Marcel van Daalen for feedback on some aspects of the Monte Carlo model for the RM pairs. This research made use of Astropy, a community-developed core Python package for astronomy (Astropy Collaboration et al. 2013) hosted at http://www.astropy.org/, of Matplotlib (Hunter 2007), of APLpy (Robitaille & Bressert 2012), an open-source astronomical plotting package for Python hosted at http://aplpy.github.com/, and of TOPCAT, an interactive graphical viewer and editor for tabular data (Taylor 2005).

## References

Akahori T., Ryu D., Kim J., Gaensler B. M., 2013, ApJ, 767, 150
Akahori T., Gaensler B. M., Ryu D., 2014, ApJ, 790, 123
Akahori T., et al., 2018, PASJ, 70, R2
Anderson C. S., Gaensler B. M., Heald G. H., O'Sullivan S. P., Kaczmarek J. F., Feain I. J., 2018, ApJ, 855, 41
Astropy Collaboration et al., 2013, A&A, 558, A33
Banfield J. K., O'Sullivan S. P., Wieringa M. H., Emonts B. H. C., 2019, MNRAS, 482, 5250
Baratta P., Bel J., Plaszczynski S., Ealet A., 2019, arXiv e-prints, p. arXiv:1906.09042
Beck R., 2015, in Lazarian A., de Gouveia Dal Pino E. M., Melioli C., eds, Astrophysics and Space Science Library Vol. 407, Magnetic Fields in Diffuse Media. p. 507, doi:10.1007/978-3-662-44625-6˙18
Beck A. M., Hanasz M., Lesch H., Remus R.-S., Stasyszyn F. A., 2013, MNRAS, 429, L60
Bi H., Davidsen A. F., 1997, ApJ, 479, 523
Blasi P., Burles S., Olinto A. V., 1999, ApJ, 514, L79
Botteon A., et al., 2018, MNRAS, 478, 885
Braun R., Bourke T., Green J. A., Keane E., Wagg J., 2015, in Advancing Astrophysics with the Square Kilometre Array (AASKA14). p. 174
Bray J. D., Scaife A. M. M., 2018, ApJ, 861, 3
Brentjens M. A., de Bruyn A. G., 2005, A&A, 441, 1217
Brown S., et al., 2017, MNRAS, 468, 4246
Burn B. J., 1966, MNRAS, 133, 67
Carilli C. L., Taylor G. B., 2002, ARA&A, 40, 319
Chuang C.-H., et al., 2015, MNRAS, 452, 686
Coles P., Jones B., 1991, MNRAS, 248, 1
Condon J. J., Cotton W. D., Greisen E. W., Yin Q. F., Perley R. A., Taylor G. B., Broderick J. J., 1998, AJ, 115, 1693
Csáki C., Kaloper N., Peloso M., Terning J., 2003, J. Cosmology Astropart. Phys., 2003, 005
Dermer C. D., Cavadini M., Razzaque S., Finke J. D., Chiang J., Lott B., 2011, ApJ, 733, L21
Dolag K., Kachelriess M., Ostapchenko S., Tomàs R., 2011, ApJ, 727, L4
Donnert J., Dolag K., Lesch H., Müller E., 2009, MNRAS, 392, 1008
Durrer R., Neronov A., 2013, A&ARv, 21, 62
Farnsworth D., Rudnick L., Brown S., 2011, AJ, 141, 191
Furlanetto S. R., Loeb A., 2001, ApJ, 556, 619
Gaensler B. M., Beck R., Feretti L., 2004, New Astron. Rev., 48, 1003
Gaensler B. M., Landecker T. L., Taylor A. R., POSSUM Collaboration 2010, in BAAS. p. 470.13
Garrington S. T., Leahy J. P., Conway R. G., Laing R. A., 1988, Nature, 331, 147
George S. J., Stil J. M., Keller B. W., 2012, Publ. Astron. Soc. Australia, 29, 214
Gheller C., Vazza F., 2019, MNRAS, 486, 981
Govoni F., et al., 2019, Science, 364, 981
Grasso D., Rubinstein H. R., 2001, Phys. Rep., 348, 163
Hackstein S., Vazza F., Brüggen M., Sigl G., Dundovic A., 2016, MNRAS, 462, 3660
Hackstein S., Brüggen M., Vazza F., Gaensler B. M., Heesen V., 2019, MNRAS, 488, 4220
Hardcastle M. J., et al., 2019, A&A, 622, A12
Harvey-Smith L., Madsen G. J., Gaensler B. M., 2011, ApJ, 736, 83
Horns D., Maccione L., Meyer M., Mirizzi A., Montanino D., Roncadelli M., 2012, Phys. Rev. D, 86, 075024

Hunter J. D., 2007, Computing In Science & Engineering, 9, 90
Hutschenreuter S., Enßlin T. A., 2019, arXiv e-prints, p. arXiv:1903.06735
Knuettel S., O'Sullivan S. P., Curiel S., Emonts B. H. C., 2019, MNRAS, 482, 4606
Kolatt T., 1998, ApJ, 495, 564
Kronberg P. P., Perry J. J., 1982, ApJ, 263, 518
Kulsrud R. M., Zweibel E. G., 2008, Reports on Progress in Physics, 71, 046901
Lacy M., et al., 2019, arXiv e-prints, p. arXiv:1907.01981
Laing R. A., 1988, Nature, 331, 149
Laing R. A., Bridle A. H., Parma P., Murgia M., 2008, MNRAS, 391, 521
Locatelli N., Vazza F., Domínguez-Fernández P., 2018, Galaxies, 6, 128
Mahatma V., Hardcastle M. J., O'Sullivan S. P., 2020, MNRAS, in preparation
Mo H., van den Bosch F. C., White S., 2010, Galaxy Formation and Evolution. Cambridge Univ. Press
Montanino D., Vazza F., Mirizzi A., Viel M., 2017, Phys. Rev. Lett., 119, 101101
Neld A., et al., 2018, A&A, 617, A136
Neronov A., Vovk I., 2010, Science, 328, 73
O'Sullivan S. P., et al., 2013, ApJ, 764, 162
O'Sullivan S., et al., 2018a, Galaxies, 6, 126
O'Sullivan S. P., Lenc E., Anderson C. S., Gaensler B. M., Murphy T., 2018b, MNRAS, 475, 4263
Oppermann N., et al., 2012, A&A, 542, A93
Oppermann N., et al., 2015, A&A, 575, A118
Oren A. L., Wolfe A. M., 1995, ApJ, 445, 624
Planck Collaboration et al., 2016a, A&A, 594, A19
Planck Collaboration et al., 2016b, A&A, 594, A13
Pshirkov M. S., Tinyakov P. G., Urban F. R., 2016, Phys. Rev. Lett., 116, 191302
Purcell C. R., et al., 2015, ApJ, 804, 22
Raffelt G., Stodolsky L., 1988, Phys. Rev. D, 37, 1237
Ravi V., et al., 2016, Science, 354, 1249
Robitaille T., Bressert E., 2012, APLpy: Astronomical Plotting Library in Python, Astrophysics Source Code Library (ascl:1208.017)
Rudnick L., 2019, arXiv e-prints, p. arXiv:1901.09074
Rudnick L., Blundell K. M., 2004, in T. Reiprich, J. Kempner, & N. Soker ed., The Riddle of Cooling Flows in Galaxies and Clusters of galaxies. p. 153
Ryu D., Kang H., Cho J., Das S., 2008, Science, 320, 909
Saripalli L., Subrahmanyan R., 2009, ApJ, 695, 156
Schnitzeler D. H. F. M., 2010, MNRAS, 409, L99
Shimwell T. W., et al., 2019, A&A, 622, A1
Smith D. J. B., et al., 2016, in Reylé C., Richard J., Cambrésy L., Deleuil M., Pécontal E., Tresse L., Vauglin I., eds, SF2A-2016: Proceedings of the Annual meeting of the French Society of Astronomy and Astrophysics. pp 271–280 (arXiv:1611.02706)
Sotomayor-Beltran C., et al., 2013, A&A, 552, A58
Stasyszyn F., Nuza S. E., Dolag K., Beck R., Donnert J., 2010, MNRAS, 408, 684
Stil J. M., Taylor A. R., Sunstrum C., 2011, ApJ, 726, 4
Stuardi C., O'Sullivan S. P., Bonafede A., Brueggen M., 2020, A&A, in preparation
Subramanian K., 2016, Reports on Progress in Physics, 79, 076901
Tavecchio F., Ghisellini G., Bonnoli G., Foschini L., 2011, MNRAS, 414, 3566
Tavecchio F., Roncadelli M., Galanti G., Bonnoli G., 2012, Phys. Rev. D, 86, 085036
Taylor M. B., 2005, in Shopbell P., Britton M., Ebert R., eds, Astronomical Society of the Pacific Conference Series Vol. 347, Astronomical Data Analysis Software and Systems XIV. p. 29
Taylor A. R., Stil J. M., Sunstrum C., 2009, ApJ, 702, 1230
Taylor A. M., Vovk I., Neronov A., 2011, A&A, 529, A144
Vacca V., et al., 2018, MNRAS, 479, 776
Van Eck C. L., et al., 2018, A&A, 613, A58
Vazza F., Ferrari C., Brüggen M., Bonafede A., Gheller C., Wang P., 2015, A&A, 580, A119

**Table 2.** Table of the coordinates, angular separation and RM values of all sources in the sample. The ID column indicates classification as a random or physical pair with the 'r' or 'p' suffix. The nominal RM error value does not include the error from the ionosphere RM correction, and thus is only valid in the case of taking the difference in RM between pairs in this catalog.

| ID | RA [J2000] | Dec [J2000] | $\Delta\theta$ [arcmin] | RM [rad m$^{-2}$] | RM error [rad m$^{-2}$] |
|---|---|---|---|---|---|
| 1p | 00:18:09.27 | 31:01:19.19 | 2.48 | −76.848 | 0.045 |
| 1p | 00:18:08.39 | 31:03:47.53 | 2.48 | −77.338 | 0.016 |
| 2p | 00:29:00.04 | 29:42:15.88 | 1.22 | −62.950 | 0.010 |
| 2p | 00:29:05.56 | 29:42:01.73 | 1.22 | −60.584 | 0.007 |
| 3p | 00:44:34.09 | 12:11:26.59 | 0.80 | −15.581 | 0.013 |
| 3p | 00:44:36.24 | 12:10:50.60 | 0.80 | −14.323 | 0.005 |
| 4p | 00:45:59.20 | 22:26:54.03 | 7.50 | −45.683 | 0.016 |
| 4p | 00:46:31.67 | 22:27:06.75 | 7.50 | −48.699 | 0.026 |
| 5p | 00:46:54.30 | 12:57:06.82 | 3.56 | −12.789 | 0.006 |
| 5p | 00:46:52.13 | 12:53:35.36 | 3.56 | −13.192 | 0.020 |
| 6r | 00:47:06.84 | 12:44:52.99 | 12.61 | −11.804 | 0.030 |
| 6r | 00:46:54.30 | 12:57:06.82 | 12.61 | −12.789 | 0.006 |
| 7p | 00:51:02.21 | 13:13:37.38 | 5.52 | −14.196 | 0.054 |
| 7p | 00:50:44.09 | 13:16:56.84 | 5.52 | −17.856 | 0.033 |
| 8r | 00:53:23.20 | 33:27:25.21 | 8.87 | −57.024 | 0.016 |
| 8r | 00:52:40.78 | 33:26:51.98 | 8.87 | −63.782 | 0.039 |
| 9p | 01:01:23.40 | 29:28:52.50 | 1.85 | −67.635 | 0.043 |
| 9p | 01:01:30.60 | 29:27:53.26 | 1.85 | −70.170 | 0.028 |

Excerpt of the full table which is available online.

Vazza F., Brüggen M., Gheller C., Hackstein S., Wittor D., Hinz P. M., 2017, Classical and Quantum Gravity, 34, 234001
Vazza F., Ettori S., Roncarelli M., Angelinelli M., Brüggen M., Gheller C., 2019, A&A, 627, A5
Vernstrom T., Gaensler B. M., Brown S., Lenc E., Norris R. P., 2017, MNRAS, 467, 4914
Vernstrom T., Gaensler B. M., Rudnick L., Andernach H., 2019, ApJ, 878, 92
Widrow L. M., 2002, Reviews of Modern Physics, 74, 775
Widrow L. M., Ryu D., Schleicher D. R. G., Subramanian K., Tsagas C. G., Treumann R. A., 2012, Space Sci. Rev., 166, 37
Williams D., 2001, Weighing the Odds: A Course in Probability and Statistics. Cambridge Univ. Press
Zweibel E. G., Heiles C., 1997, Nature, 385, 131
de Gasperin F., Mevius M., Rafferty D. A., Intema H. T., Fallows R. A., 2018, A&A, 615, A179
de Gasperin F., et al., 2019, A&A, 622, A5
van Haarlem M. P., et al., 2013, A&A, 556, A2
van Weeren R. J., de Gasperin F., Akamatsu H., Brüggen M., Feretti L., Kang H., Stroe A., Zandanel F., 2019, Space Sci. Rev., 215, 16